Human gaze is precisely aligned with the foveolar cone topography of both eyes

Authors and affiliation

Jenny L. Reiniger, Niklas Domdei, Frank G. Holz, Wolf M. Harmening*

Department of Ophthalmology, Rheinische Friedrich-Wilhelms-Universität Bonn, Bonn, Germany

* Corresponding author: Wolf M. Harmening, wolf.harmening@ukbonn.de

Abstract

The small physical depression of the human retina, termed fovea, is the functional center of human vision, providing an acute sense of visual space and color, but it is yet unclear if the exact arrangement of the few thousand photoreceptors at the foveal center is relevant for visual behavior. By employing adaptive optics *in vivo* imaging and micro-stimulation, we created complete topographical maps of the foveolar cone mosaics in both eyes of 20 healthy participants while simultaneously recording the exact retinal location of a fixated visual object in a psychophysical experiment. We found that the locus of fixation was systematically shifted away from the topographical centers towards a naso-superior quadrant of the foveolea in both eyes, thereby creating an enlarged binocular area of visual space sampled by high density cones. This demonstrates a finely tuned link between the development of the cellular arrangement of the photoreceptors of the foveola and visual behavior.

Introduction

As a sensory organ, the human eye is a highly dynamic optical probe that projects sharp images of the environment onto the retina, the light sensitive tissue of the brain. As the entry point of neural activity initiating our rich and acute sense of vision, the retina contains about 100 million photoreceptors (*1*) which sample the retinal image over space and time. The spatial distribution and arrangement of these cells across the retina is strikingly non-uniform, with a concentration of tightly packed cone photoreceptors at a small, centrally located circular area, termed fovea, because of its anatomical feature as a shallow physical depression within the surrounding retinal tissue. At the center of the fovea, the foveola, downstream neurons are displaced centrifugally to allow an un-obstructed illumination of the cones, maximizing optical fidelity by reduced light scatter. The natural variation in foveal size and cone axon length in primates are optimized to the cells' biophysical capabilities and limitations, providing an essentially loss-free transmission of electrical signals through elongated axons (*2*). While the foveal pit already forms during fetal development, the main elongation and migration of cones, accompanied by a thickening of the outer nuclear layer in the very center of the fovea, takes place after birth and in the early years of child development (*3*, *4*). Those morphological changes are accompanied by enhancements in visual capacity during development, such as cortical processes, orientation and directional selectivity, eye movements and fixation, as well as spatial frequency tuning (*5*). For high acuity vision, for instance during reading small print, only the smallest and most densely packed cells are employed at the foveola. Here, in an area free of rods or vascular structure, cone density peaks at about 160,000 cones/mm^2 (*6*). What is unknown yet is to what extend the cellular mosaic of foveolar cones in an individual bear on visual function and behavior. Human gaze behavior is a dynamic, binocular controlled process, with an ongoing alternation of gaze shifts and fixations. During fixation, small, involuntary and subconsciously performed residual eye motions are constantly present, termed fixational eye movements (FEMs), which are essential for a variety of visual functions. FEMs, especially microsaccades, indicate the orientation of visual attention, relocate the gaze within the foveola (*7*, *8*) and prevent the object of interest from fading (*9*). Visual resolution acuity also benefits from retinal motion across the stimulus and was shown to decrease when the retinal image is stabilized by matching the motion of a stimulus to the eye's concurrent motion (*10*, *11*). The center of retinal locations used in a fixation task is, in general, referred to as the preferred retinal locus of fixation (PRL). Different groups independently found that this functional center does not colocalize with the peak of cone density distribution and other anatomical features of the foveal pit (*6*, *12–16*). However, due to small participant populations, monocular measurements or indirect methods of PRL estimation, little is known about the nature of this

displacement and a systematic analysis of binocular fixation locations has not been performed so far.

Advances in adaptive optics scanning laser ophthalmoscopy during the past decade now enable us to resolve the complete mosaic of cone photoreceptors at the foveal center and, by utilizing adaptive optics microstimulation techniques, to track the retinal landing point of a visual stimulus with subcellular resolution. We here take advantage of this experimental access to the cellular basis of human vision, and first characterize the binocular cellular structure of the cone photoreceptor mosaic in the eyes of 21 healthy individuals, and then relate this structural organization to the individual's visual fixation behavior, a key functional performance of the eye.

Results

Topography of the foveolar cone mosaic

By high-resolution adaptive optics scanning laser ophthalmoscopy (AOSLO), binocular cone photoreceptor topography at the very center of the fovea was analyzed in 41 eyes of 21 healthy human participants. In each retinal image, about 6800 to 9100 individual cones were resolved, marked and their location used to compute continuous two-dimensional maps of cone density (see Methods, Fig. 1A-F). Cone density distribution in the central 0.85 x 0.85 deg field of view (corresponding to between 218 and 253 µm on the retina) varied highly across participants, and was highly correlated between fellow eyes (Fig. 1I). One of the most common metrics of interest is the peak cone density (PCD). The PCD in participants who were tested binocularly was on average 13,995 and 13,940 cones/deg^2 in right and left eyes, respectively (range$_{right}$: 10,823 – 16,217 cones/deg^2, range$_{left}$: 10,894 – 17,309 cones/deg^2). Taking the individual retinal magnification factors (261 – 304 µm per degree of visual angle) into account, these corresponded to linear average densities of 182,528 and 182,675 cones/mm^2 in right and left eyes, respectively, (range$_{right}$: 148,503 – 212,760 cones/mm^2, range$_{left}$: 145,870 – 217,811 cones/mm^2). The highest angular cone density (18,023 cones/deg^2, 221,889 cones/mm^2) was observed in the right eye of the only participant of whom the left eye's foveolar mosaic could not be resolved completely, therefore those data were not included in any binocular analyses. Overall, the differences between PCD in fellow eyes were not significant (paired t-test, $p = 0.6$). The PCD difference in fellow eyes was on average 403 cones/deg^2 (which equals 3 % of the PCD). Grouping by ocular dominance, i.e., by the eye which is preferred subjectively in vision tasks, there was no significant difference in PCD between dominant and non-dominant eyes (paired t-test, $p = 0.4$). The PCD in dominant eyes was higher for 60 % of the participants.

The retinal location of peak cone density is prone to high variability when comparing the AOSLO images recorded on different days, for instance, because of slightly varying image distortions as a result of eye motion, image noise and the resulting variance in marked cone center locations. Thus, a novel spatially invariant metric for reporting the topographical center of the fovea was introduced. The cone density centroid (CDC), computed as the weighted center of cone density values within the 20th percentile contour (Fig. 1F), was used as spatial reference location to define other functionally relevant locations in the foveola. For 8 participants (16 eyes), the foveolar cone mosaic was imaged and analyzed on two different days. After careful alignment of cone-resolved high signal-to-noise ratio images, the comparison of PCD and CDC locations on different days, showed a larger distance between PCD locations (mean ± std: 3.0 ± 2.3 arcmin, range: 0.1 – 7.9 arcmin). The distances between CDC locations were significantly (paired t-test, $p = 0.002$) smaller (mean ± std: 0.9 ±

0.7 arcmin, range: 0.1 – 2.6 arcmin). The cone densities at CDC locations ranged between 10,692 and 16,997 cones/deg^2 (143,232 to 215,550 cones/mm^2) and differed from the PCD by an average of 3 % (std: ± 2 %). The density at both locations, PCD as well as CDC also showed a very strong correlation in fellow eyes ($r^2 = 0.95$, $p << 0.001$ and $r^2 = 0.89$, $p << 0.001$, respectively), (Fig. 1G). Throughout this work, we define the CDC as 0 deg eccentricity.

Cone density decreased rapidly with eccentricity with a slightly steeper slope in the vertical meridian (Fig. 1G, H). The standard deviation of the density distribution across participants was highest in the center of the distribution and decreased to about 2/3 of the central variation towards ± 20 arcmin eccentricity (Fig. 1G). Normalization of the data to the cone density at CDC visualized the slight differences and showed that we not always measured the highest cone density value at the center of the density distribution. In the horizontal and vertical meridian, cone density decreased to about 71 % and 65 % of the CDC density at ± 20 arcmin of eccentricity, respectively (Fig. 1G).

Interocular symmetry of foveolar cone mosaics

We noticed that during the analysis of all foveolar cone topography maps, it seemed possible to find – by eye – fellow eye data in a scrambled arrangement of all such maps (see Fig. S1), possibly due to similarities in absolute density and a mirror symmetry between both foveolae. To quantify mirror symmetry, three different analysis were performed: (1) spatial two-dimensional differences (or reproducibility) of cone density maps of the same eye, recorded and analyzed independently on different days (columns in Fig. 2A, B), (2) difference between density maps of fellow eyes which were recorded on the same day (rows in Fig. 2A, B), and (3) the difference between individual density maps and the overall average density map, calculated as an average of left and right eyes independently of all participants (Fig. 2C). To quantify the two-dimensional differences, the root-mean-square (RMS) of the point-by-point difference maps was used for the comparison between absolute and normalized density maps (Fig. 2D and E, respectively, compare with Fig. 1H and J). The first analysis, comparing density maps of the same eyes over time, revealed a median RMS of about 2.9 % between measurements (range: 1.5 – 5.9 %).

The RMS of differences between fellow eyes were about 1.0 % higher (median RMS: 3.8 %) and ranged between 2.6 and 6.9 %. The comparison between individual eyes and the mean density maps of all participants showed significantly higher differences (median: 8.7 % range: 3.4 – 23.1 %), that occurred mainly due to the large variation in absolute density values among participants (Fig. 2D).

To allow for a better comparison of the two-dimensional shape, the density maps were normalized to the density at the CDC. The analysis of reproducibility again showed the smallest variance between density maps from the same eye (median RMS: 2.1 %, range: 1.4 – 5.6 %). The normalization of density maps resulted in an approximation of the RMS of differences between normalized individual vs. average density maps (median RMS: 4.0 %, range: 1.9 – 12.9 %) and the normalized differences between fellow eyes (median RMS: 3.3 %, range: 1.8 – 8.9 %).

Fixation behavior is extremely fine-tuned and reproducible

The optimal retinal locus, termed preferred retinal locus of fixation (PRL), and fixation stability were derived in each eye by extracting the landing position of a small visual target during AOSLO microstimulation. (Fig. 3A, B). The exact stimulus positions relative to cone locations were determined by registering the experiment's video data with the high signal-to-noise image used for cone annotation. On each measurement day, five videos were recorded consecutively, with short breaks in between. Measurements were generally highly reproducible between consecutive measurements with a median distance between PRLs of 2.2 arcmin (range: 1.0 - 5.6 arcmin) (Fig. 3C, F). When pooling all stimulus locations from a single day (≥ 3 x 150 video frames pooled), median locations differed by 1.5 arcmin (range: 1.0 - 4.2 arcmin) (Fig. 3D, F). The observed fixation stability, given by the bivariate contour ellipse areas, BCEA, ranged between 23 and 136 arcmin^2 in right (mean ± std: 66 ± 30 arcmin^2) and between 30 and 132 arcmin^2 in left eyes (mean ± std: 69 ± 23 arcmin^2). The orientation, size and location of the BCEAs were very similar across days (Fig. 3 C). Across participants however, BCEAs showed large variability, but they were strongly correlated between right and left eyes of each participant ($r^2 = 0.66$, $p << 0.001$) (Fig. 3D). When grouping eyes according to ocular dominance, there was no difference between BCEAs of dominant and non-dominant eyes ($p = 0.052$, Wilcoxon signed rank test, $n = 20$). The participants who had a larger median BCEA showed a significant trend to have a higher variation range between single measurements than participants who had a small BCEA ($\rho = 0.48$, $p = 0.002$) (Fig. 3D). In the majority of the eyes studied (33/41), fixation behavior was examined on two or more days (see Table S1). Additionally, in the right eyes of two of the trained participants (P 4 and 21), PRL videos were recorded over a period of 3.5 years, in 12 and 17 experiment sessions, respectively (Fig. S2A). The location of the PRL was extremely stable even across multiple years, with an average location difference of 1.2 and 1.5 arcmin for P21 and 4, respectively, corresponding to a distance on the retina of one to three foveolar cone diameters.

Fixation is offset naso-superiorily relative to cone topography center

Because both the location of the CDC and that of the PRL showed such high reproducibility over time, it was possible to study their relationship to each other. The CDC locations were covered by the BCEA in 15 of 40 eyes (≙ 37.5 %). When plotting the fixation ellipses relative to the CDC for right and left eyes of all participants, a mirror symmetrical offset towards the naso-superior quadrant emerged (Fig. 4A). Only in one participant (P18) both PRLs were offset temporally. The angular distance between the CDC and the PRL was on average 4.5 and 5.0 arcmin in right and left eyes, respectively. Distances in fellow eyes were strongly correlated ($r^2 = 0.41$, $p = 0.002$, Fig. S3A), which were likely a result of the strong correlation in the vertical direction ($r^2 = 0.72$, $p << 0.001$, Fig. 4B). Horizontal offsets showed a larger variation between fellow eyes and were not significantly correlated ($r^2 = 0.05$, $p = 0.32$). Also, the offset's angular component was not significantly correlated ($r^2 = 0.05$, $p = 0.36$), albeit with a mirror symmetrical trend (Fig. S3C). The same trend in offsets of the PRL could be found when reanalyzing the data from Wang et al., 2019 (*6*) with our analysis methods (Fig. S3). Fixation stability, given by the BCEA, did not show a correlation to the PRLs offset distance from the CDC ($\rho = -0.01$, $p = 0.94$).

We make the assumption that the same PRLs are used under monocular and binocular viewing conditions and that PRLs are retinal coordinates of corresponding points in the visual environment and therefore fixed positions independently of viewing distance (*17*). With the PRLs of both eyes as common center, the topographical centers of cone density are primarily offset horizontally in the visual field (Fig. 5A). In this projection, the CDCs of right eyes landed left-hand from the left eye's CDCs. This was reversed in four participants, likely due to a minimal horizontal offset component. The same high cone density areas that were used for defining the CDC location were chosen to visualize the overlap between both eyes' high-density sampling areas in the visual field. Given the interindividual variations of cone topography, this yielded an overall orbital distribution that was, on average, shifted to being centered slightly above the fixated target (Fig. 5B and C). Cone densities at the rim of these binocular fields ranged between 9600 and 14900 cones/deg^2, roughly equaling the highest 13 % of cone densities across the entire retina, considering previously reported cone densities at larger retinal eccentricities (*1*, *18*). The Nyquist limit of sampling within those areas was < 35 arcsec, equaling 20/13 vision or better. The illustration of a computer reading scene in Fig. 5D serves as a simplified static visualization of the geometry and magnitude of the average offsets between fellow eyes. In reality, reading is a high-dynamic process with ongoing crossing and uncrossing of the line of sights. For the case of steady fixation, the union of both eyes' high cone density areas results in a horizontally enlarged area of supreme visual sampling.

Discussion

With refined optical and analytical tools, we find a systematic relationship between foveolar cone topography and fixation behavior in both fellow eyes of 20 observers. We reveal that the mirror symmetry of cone topography between fellow eyes is also reflected in the location of the PRL, the preferred retinal locus of fixation, which is slightly offset to the location of maximum density of foveolar cones. These offsets between retinal structure on the one hand and visual behavior on the other hand, while being idiosyncratic in amplitude and direction between observers, share a common pattern: high cone density areas are spread across the binocular visual field horizontally, on average, thereby enlarging the area of the visual field sampled by the most accurate spatial detectors that both eyes can offer.

Foveolar cone topography

A variety of metrics can be used to describe foveolar cone topography. The peak cone density (PCD), in addition to describing the densest measurable accumulation of photoreceptors, is commonly used to define the anatomical center of the foveola. The PCDs observed here, varied widely across participants and show a similar range as in previous studies (*6*, *12*, *13*, *15*, *18–21*). However, the highest densities reported were found in histological data (*1*). In alignment with histology and two *in vivo* imaging studies (*1*, *6*, *19*), we found a steeper drop in human cone density across the vertical compared to the horizontal meridian (Fig. 1G,H), similar as is described in the retinas of other mammals (*22*, *23*). Differences in cone densities measured between studies can result from e.g. the examined population, optical differences in the imaging pathway, imaging wavelength, postprocessing and averaging of the data and different methods that underly cell density calculation, as well as sample preparation (for histological tissue). A detailed discussion of those factors can be found in the report by Wang et al. (2019) (*6*). The fact that more and more optical and analytical limitations are lifted with novel imaging techniques, like sub diffraction-limited resolution offered by AOSLO (*24*), leads towards a replacement of the gold standard for quantitative cone mosaic analysis, from histology of dissected tissue preparations towards high resolution *in vivo* imaging.

The three children who participated in the study were aged 10, 12 and 14 (P3, P10 and P16, respectively) and did not show differences from the adult population in peak cone density or cone density symmetry. Previous studies, examining the cone photoreceptor density between 0.2 mm and 1.5 mm eccentricities, found no correlation between cone densities and age for participants between 10 and 69 years (*25*) and for children between 5.8 and 15.8 years (*26*). Our results extend those findings into the foveal center. Histological studies point to an earlier cease of centripetal cone photoreceptor migration, with a doubling of cone density between

22 weeks of gestation and 5 days postnatal examinations and a tripling between 5 days and 45 months post-natal (*3*). With 108,439 cones/mm^2, the cone density at the age of 45 months equates to about 60% of the mean cone density, 183,560 cones/mm^2, found in our population. However, visual acuity in children was shown to approach those observed in adults between the age of 5 and 6 years (*27*). Thus, the children examined here are assumed to be in a comparable stage of visual development as adults.

Interocular symmetry

Symmetry is an extensively studied characteristic in various organs. Previous observations in the field of ophthalmic optics showed ocular symmetries between fellow eyes, such as corneal topography and ocular wavefront aberrations (*28*). Moreover, a high interocular correlation between cone densities was shown for different retinal eccentricities (250, 420, 760 and 1300 µm) (*29*). A later evaluation of cone density symmetry, that also included PCD values, confirmed those results (*19*). A recent study carefully compared interocular cone density maps in the foveal center, similar to our data. Cava et.al. found that, in addition to the PCD, the Voronoi cell area regularity and certain iso-density contour areas are also highly symmetrical between fellow eyes (*21*). Here, we also observed a high symmetry between cone density maps of fellow eyes, with a difference in topography between fellow eyes which was just slightly lower than the difference between two independently analyzed cone mosaic maps of the same eye. The observed differences arise because of slightly different shapes of the mosaics, which are likely to be anatomically present. One has to keep in mind that due to the scanning nature of the AOSLO, associated with a pixelwise image acquisition and sequential stabilization process, small image distortions could have been introduced. With an expected magnitude of up to 3 pixels (≙ 0.3 arcmin), such image distortions are minor compared to the magnitude of measured offsets. By manually selecting a reference frame with low distortions, we further minimized this confound.

The comparison between normalized individual cone density maps and averaged maps shows that the general shape of the central cone density distribution is similar across participants. Nevertheless, some eye pairs appear to have a more particular shape than the average. Those might be underrepresented by evaluating the RMS of the whole density map and could be investigated in more detail (Fig. S1). PCDs in fellow eyes had a very strong correlation and no difference between right and left eyes could be observed, as also discussed by Cava et al. (*21*). Some preliminary data from our group suggested that resolution acuity seemed to be better in the dominant eyes of all 5 examined participants (also included here), while acuity thresholds were highly correlated with the density of the foveolar cone mosaic (*30*). When comparing dominant eyes to non-dominant eyes in our

population, there is no significant difference in PCDs, which might be due to the particular retinal locations that are used during the resolution task. To prove this hypothesis, resolution acuity and ocular dominance need to be investigated in a larger population. Additionally the knowledge of ocular aberrations might help to better understand how optical limits during development influence the formation of the optimal retinal locus, as they affect the sampling limit for resolution tasks (*31*).

As another functional correlate, we studied fixation stability in fellow eyes, which was quantified using the BCEA. BCEAs of fellow eyes were highly correlated, which supports the general hypothesis of an underlying coupling of both eyes, an effect visible even under monocular viewing conditions. Previous studies found comparable microsaccade rates and amplitudes in fellow eyes under monocular viewing conditions (*32*), as well as correlating 95 % BCEAs between right and left eyes, measured with a clinical microperimetry system (*33*) and suggest an improved fixation stability under binocular viewing conditions (*32*, *34*).

Preferred retinal locus of fixation

In the natural environment, fixation, discrimination or resolution requirements are often closely related. For a long time, it was common view that the anatomical center of the fovea also represents the center of fixation (*35*), a view supported by the rough alignment between these retinal loci. With current imaging techniques, opening the door to the exact cellular makeup of an individual eye however, it was revealed that the PRL is offset from the location of the PCD as well as the center of the foveal avascular zone and the foveal pit (*6*, *12–15*). Our study confirms the offset between PRL and PCD and shows that it differs from the location of the CDC as well (as a better reproducible metric for describing the center of cone density distribution). As recently shown, the PRL is also offset from other functionally relevant foveolar locations that provide the highest sensitivity to small spot stimuli (*36*).

The PRL proves to be very reproducible over a period of at least 3.5 years (Fig. S2A), which confirms and extends the finding of Kilpeläinen et al., who show the PRL to be reproducible over a period of two days, on average (*14*). Small differences in PRL variation between days (Kilpeläinen et al.: 0.52 arcmin; this study: 1.2 arcmin) might be observed because of differences in the fixational tasks.

Kilpeläinen et.al. used a moving target, possibly providing higher fixation stability due to a higher attentional demand for the participant (*16*). The observed offset of the PRL compared to the CDC location (mean: 4.8 arcmin; PRL to PCD: 5.2 arcmin) was similar to the presented distances between PRL and PCD in the study of Kilpeläinen et.al. (mean: 5.08 arcmin) and corresponds to a distance of about 10 cone diameters. Other studies found larger offsets with median values of 9.8 and 11.5 arcmin (*12*, *13*). Offset measurements are most likely

influenced by the study specific parameters, such as a low number of subjects or a less accurate method of measuring the PRL.

Nevertheless, all studies show a trend of the PRLs to be formed superior to the PCD/CDC. Examining both fellow eyes of two larger populations (40 and 24 eyes), we here found the PRL to have a, in fundus view, preferably naso-superior offset from the CDC in right and left eyes. Therefore, the center of cone density distribution is slightly offset towards a top nasal direction in relation to a fixated target in the visual environment. In a scenario of computer work involving reading the display at 70 cm distance, this offset roughly equals the distance between two letters (Times New Roman, fontsize 12, 100% magnification, ≙ 1 mm). The offsets between eyes are, on average, mirror symmetric between eyes in a way such that the right eye's CDC sits at a letter left of fixation, and the left eye's CDC on the one right of fixation.

A static projection of PRLs and CDCs to the visual environment illustrates the horizontal enlargement of a high cone density area in the cyclopean view. By the rules of binocular combination, the eye that sees a higher contrast and sharper details gets more weight in the cyclopean percept (*37*). Therefore, in binocular combination of high cone density areas an advantaged emerges over a perfectly aligned topography and fixation.

This highly ordered and systematic architecture between fellow eyes could be the result of a developmental process creating appropriate location information for binocular spatial sampling. One of the factors driving the enrichment of visual capacities during development is the demand of resolving fine structures in the visual environment. The PCD seems to only be a circumstantial factor as there was no distinct relation to the PRLs offset observed across populations. The topography of retinal connectivity within the foveolar midget circuit might be one of the more important driving factors of PRL formation. The connectivity between individual cones and midget bipolar and ganglion cells was recently shown to develop and establish a private line for the central photoreceptors already during gestation (*38*). The centripetal migration of cone photoreceptors starts in parallel, but mainly takes place after birth (*3*). The nasal superior direction supports the closest connectivity to the optic nerve head, which could facilitate the slightly offset PRL development, even if conduction velocity of retinal ganglion cells was shown to minimize possible time differences among the retina (*39*). In higher retinal eccentricities, midget ganglion cells have been shown to have smaller dendritic field diameters in the nasal quadrant of human retinae (*40*), which may be driven by the same underlying mechanisms as PRL formation.

Conclusions & outlook

Taken together, participants without known retinal disease or abnormalities showed a small but systematic offset between their PRL and the center of cone density distribution, formed in a way to enlarge the area of high cone densities in the binocular visual field. This functional symmetry was associated with a high interocular symmetry of foveolar cone topography. Binocular, foveated display systems that seek to mimic human vision with high precision could be tuned to reflect this spatial relationship (*41*). Acquired retinal disease as well as developmental abnormalities or asymmetries in ocular biometry could be indicated by observed interocular differences or deviations in foveal topography. *In vivo* foveal topography data may provide a basis for detecting changes in the central photoreceptor topography during retinal disease (*42*), and more generally, could contribute to replace histology as the gold standard for normative human photoreceptor evaluations in a healthy population.

Materials and Methods

Participants

Forty-one eyes of twenty-one participants (7 male, 14 female, 38 adults [age: 18 – 42], 3 children [age: 10, 12 and 14]) with no known ocular conditions and only mild refractive errors (SE: ± 2.5 diopters) were studied. Participants are referred to throughout the manuscript with a singular ID, selected based on a descending order of peak cone densities for the left eye. For one of the participants (P21), data from the right eye were included as the only monocular dataset in the study, because the left eye's cone mosaic could not be resolved completely. Therefore, this eye's data were only used for PRL reproducibility analysis, as image and functional data were collected over multiple years. Most of the participants were examined on multiple days (compare Table S1). Participants P18, P4, and P21 were trained AOSLO observers and members of the lab. Mydriasis was established by two drops of 1% Tropicamide, instilled into the eyelid about 15 and 10 minutes prior to the imaging session. A third drop was administered in case imaging and experimentation continued for more than 30 minutes. A customized dental impression mold (bite bar) was used to immobilize and adjust the head position and thus to align the participants eye in front of the imaging system. Written informed consent was obtained from each participant and all experimental procedures adhered to the tenets of the Declaration of Helsinki, in accordance with the guidelines of the independent ethics committee of the medical faculty at the Rheinische Friedrich-Wilhelms-Universität of Bonn.

Adaptive optics retinal imaging

In vivo images of the complete foveolar cone mosaic were recorded using a custom built adaptive optics scanning laser ophthalmoscope (AOSLO). The general setup of the AOSLO has been described previously (*43*, *44*), pertinent differences are described here. Briefly, the AOSLO front-end featured three f = 500 mm afocal telescopes, designed to point-scan an adaptive optics corrected focal spot of light across the retina to achieve diffraction limited resolution performance in both the incident and reflected beams. A magnetic actuator-driven deformable mirror with continuous membrane surface (DM97-07, 7.2 mm pupil diameter, ALPAO, Montbonnot-Saint-Martin, France) was placed in a retinal conjugate plane and driven by the error signals of a 25x25 lenslet Shack Hartmann sensor (SHSCam AR-S-150-GE, Optocraft GmbH, Erlangen, Germany). Imaging and wavefront correction wavelength was either 840 nm (± 12 nm) or 788 nm (± 12 nm) light, obtained by serial dichroic and bandpass filtering of a supercontinuum source (SuperK Extreme EXR-15, NKT Photonics, Birkerød, Denmark). The imaging field of view was 0.85 x 0.85 degree of visual angle. The light reflected from the retina was captured in a photomultiplier tube (PMT, H7422-50, Hamamatsu

Photonics, Hamamatsu, Japan), placed behind a confocal pinhole (Pinhole diameter = 20 µm, equaling 0.47 (840nm) and 0.5 (788nm) Airy disk diameters). The PMT signal was sampled continuously in a field programmable gate array (FPGA), rendering a 512 x 512 pixel video at 30 Hz (600 pixel per degree of visual angle). With fast acousto-optic modulation of the imaging wavelengths, the square imaging field becomes a retinal display in which psychophysical visual stimulation was possible (*45*, *46*). The best images during PRL recordings (see below) where used to create spatially registered, high signal to noise ratio images of the foveal center in which all cones could be resolved.

Image processing and cone density analysis

Acquired AOSLO video frames were spatially stabilized by real-time, strip-wise image registration in custom written software (*47*). These online-stabilized videos contained frames displaying incomplete stabilization that could be due to poor image quality, eye blinks, drying tear film, etc. Such frames were identified and deleted manually. The remaining frames were averaged to obtain a single high-quality image of each retina per video. The single best of at least five such images was selected to be used for further analysis and serve as high signal-to-noise anchor image for spatial alignment with functional data recordings. All cone center locations were labeled in a semi-manual process by a single trained image grader: first, a convolutional neural network (*48*), CNN, was trained to locate cone center locations with a smaller subset of only manually graded images in our pilot study. Then, all retinal images were annotated by the newly trained CNN, and manually corrected using custom software. Such corrections were especially necessary in the foveal center, and wherever cones appeared completely dark (*49*). The manual correction prioritized mosaic regularity in cases of ambiguity (*1*). Based on the labeled cone center locations, a Voronoi tessellation was computed (MATLAB functions: *delaunayTriangulation*, *voronoiDiagram* and *voronoin*). Each cone was regarded as occupying the space of each corresponding Voronoi cell. Angular cone density (cones/deg^2) was computed at each image pixel by averaging the Voronoi area of the nearest 150 encircled cones around that pixel (Fig. 1D). Linear cone densities were computed with respect to the individual retinal magnification factors of each eye, considering axial length, anterior chamber depth and corneal curvature (*15*), based on swept source biometry (IOLMaster 700, Carl Zeiss Meditech, Jena, Germany). This method ensured smooth cone density maps and prevented sampling artifacts as they often occur using defined shapes of masks (e.g. circular or square masks) for selection of cones in a particular area (Fig. 1E). Finally, the cone density centroid (CDC) was determined as the weighted centroid (MATLAB function: *regionprops*) of the highest 20 % of cone density values. The CDC is visualized as a red circle with white fill throughout the manuscript.

The reproducibility or symmetry between cone density maps was analyzed for: the same eyes on two different days (alignment of mosaic images), fellow eyes imaged on the same day (left eyes were flipped along the vertical axis and centered on the CDC) and individual eyes against the mean cone density map of all eyes (the mean density of all right eyes was compared against the flipped density maps of individual left eyes and vice versa) (Fig. 2).

Determination of the preferred retinal location of fixation (PRL)

Using the AOSLO as stimulation platform, a small (nominal 1.6 arcmin), flashing (3 Hz) square with negative contrast polarity (light turned off) was presented as visual target at the center of the AOSLO imaging raster during image acquisition, and participants were asked to fixate the target as accurately and relaxed as possible. At least five 10-second AOSLO videos were recorded in each eye during such fixation epochs. Due to the nature of the AOSLO, the visual stimulus is directly visible with respect to the retina (Fig. 3A-B). Thus, fixation behavior can be directly and unambiguously observed in such videos. The PRL was calculated as the median fixation target location across all videos. To bring fixation behavior into spatial correspondence with the topographical analysis, averaged retinal images derived from both analysis independently were carefully aligned with each other. In 33 of the 41 eyes, PRL measurements were conducted multiple times (e.g. if participants also took part in other experiments). In three eyes, data were obtained in 8, 12 and 17 measurement sessions, respectively, over a period of 3.5 years. For eight participants (16 eyes) sessions were repeated after 1 year. For quantification of fixation stability, the bivariate contour ellipse area (BCEA), which contains one standard deviation of the data was fitted to the scatterplot of all stimulus positions (Fig. 3C).

References and Notes

1. C. A. Curcio, K. R. Sloan, R. E. Kalina, A. E. Hendrickson, Human photoreceptor topography. *J. Comp. Neurol.* **292**, 497–523 (1990).
2. G. S. Bryman, A. Liu, M. T. H. Do, Optimized Signal Flow through Photoreceptors Supports the High-Acuity Vision of Primates. *Neuron*. **108**, 335-348.e7 (2020).
3. C. Yuodelis, A. Hendrickson, A qualitative and quantitative analysis of the human fovea during development. *Vision Res.* **26**, 847–855 (1986).
4. A. Hendrickson, D. Possin, L. Vajzovic, C. A. Toth, Histologic Development of the Human Fovea From Midgestation to Maturity. *Am. J. Ophthalmol.* **154**, 767-778.e2 (2012).
5. O. Braddick, J. Atkinson, Development of human visual function. *Vision Res.* **51**, 1588–1609 (2011).
6. Y. Wang, N. Bensaid, P. Tiruveedhula, J. Ma, S. Ravikumar, A. Roorda, Human foveal cone photoreceptor topography and its dependence on eye length. *Elife*. **8** (2019), doi:10.7554/eLife.47148.
7. R. Engbert, R. Kliegl, Microsaccades uncover the orientation of covert attention. *Vision Res.* **43**, 1035–1045 (2003).
8. H. K. Ko, M. Poletti, M. Rucci, Microsaccades precisely relocate gaze in a high visual acuity task. *Nat. Neurosci.* **13**, 1549–1554 (2010).
9. S. Martinez-Conde, S. L. Macknik, X. G. Troncoso, T. A. Dyar, Microsaccades counteract visual fading during fixation. *Neuron*. **49**, 297–305 (2006).
10. K. Ratnam, N. Domdei, W. M. Harmening, A. Roorda, Benefits of retinal image motion at the limits of spatial vision. *J. Vis.* **17**, 30 (2017).
11. J. Intoy, M. Rucci, Finely tuned eye movements enhance visual acuity. *Nat. Commun.* **11**, 1–11 (2020).
12. N. M. Putnam, H. J. Hofer, N. Doble, L. Chen, J. Carroll, D. R. Williams, The locus of fixation and the foveal cone mosaic. *J. Vis.* **5**, 632–9 (2005).
13. M. A. Wilk, A. M. Dubis, R. F. Cooper, P. Summerfelt, A. Dubra, J. Carroll, Assessing the spatial relationship between fixation and foveal specializations. *Vision Res.* **132**, 53–61 (2017).
14. M. Kilpeläinen, N. M. Putnam, K. Ratnam, A. Roorda, The Anatomical, Functional and Perceived Location of the Fovea in the Human Visual System. *SSRN Electron. J.* (2020), doi:10.2139/ssrn.3699785.
15. K. Y. Li, P. Tiruveedhula, A. Roorda, Intersubject variability of foveal cone photoreceptor density in relation to eye length. *Invest. Ophthalmol. Vis. Sci.* **51**, 6858–67 (2010).

16. N. R. Bowers, J. Gautier, S. Lin, A. Roorda, Fixational eye movements depend on task and target (under review).
17. J. M. Hillis, M. S. Banks, Are corresponding points fixed? *Vision Res.* **41**, 2457–2473 (2001).
18. E. M. Wells-Gray, S. S. Choi, A. Bries, N. Doble, Variation in rod and cone density from the fovea to the mid-periphery in healthy human retinas using adaptive optics scanning laser ophthalmoscopy. *Eye*. **30**, 1135–1143 (2016).
19. T. Zhang, P. Godara, E. R. Blanco, R. L. Griffin, X. Wang, C. A. Curcio, Y. Zhang, Variability in Human Cone Topography Assessed by Adaptive Optics Scanning Laser Ophthalmoscopy. *Am. J. Ophthalmol.* **160**, 290-300.e1 (2015).
20. R. F. Cooper, M. A. Wilk, S. Tarima, J. Carroll, Evaluating Descriptive Metrics of the Human Cone Mosaic. *Investig. Opthalmology Vis. Sci.* **57**, 2992 (2016).
21. J. A. Cava, M. T. Allphin, R. R. Mastey, M. Gaffney, R. E. Linderman, R. F. Cooper, J. Carroll, Assessing Interocular Symmetry of the Foveal Cone Mosaic. *Investig. Opthalmology Vis. Sci.* **61**, 23 (2020).
22. O. Packer, A. E. Hendrickson, C. A. Curcio, Photoreceptor topography of the retina in the adult pigtail macaque (Macaca nemestrina). *J. Comp. Neurol.* **288**, 165–183 (1989).
23. K. C. Wikler, R. W. Williams, P. Rakic, Photoreceptor mosaic: Number and distribution of rods and cones in the rhesus monkey retina. *J. Comp. Neurol.* **297**, 499–508 (1990).
24. R. Lu, N. Aguilera, T. Liu, J. Liu, J. P. Giannini, J. Li, A. J. Bower, A. Dubra, J. Tam, In vivo sub-diffraction adaptive optics imaging of photoreceptors in the human eye with annular pupil illumination and sub-Airy detection. *Optica*. **8**, 333–343 (2021).
25. S. P. Park, J. K. Chung, V. Greenstein, S. H. Tsang, S. Chang, A study of factors affecting the human cone photoreceptor density measured by adaptive optics scanning laser ophthalmoscope. *Exp. Eye Res.* **108**, 1–9 (2013).
26. H. Mirhajianmoghadam, A. Jnawali, G. Musial, H. M. Queener, N. B. Patel, L. A. Ostrin, J. Porter, In vivo assessment of foveal geometry and cone photoreceptor density and spacing in children. *Sci. Rep.* **10**, 1–14 (2020).
27. Y. H. Lai, H. Z. Wang, H. T. Hsu, Development of visual acuity in preschool children as measured with Landolt C and Tumbling e charts. *J. AAPOS*. **15**, 251–255 (2011).
28. J. Francisco Castejón-Mochón, N. López-Gil, A. Benito, P. Artal, Ocular wave-front aberration statistics in a normal young population. *Vision Res.* **42**, 1611–1617 (2002).
29. M. Lombardo, G. Lombardo, D. Schiano Lomoriello, P. Ducoli, M. Stirpe, S. Serrao, Interocular symmetry of parafoveal photoreceptor cone density distribution. *Retina*. **33**, 1640–9 (2013).
30. J. L. Reiniger, N. Domdei, M. Linden, F. G. Holz, W. M. Harmening, in *Investigative*

Opthalmology & Visual Science (ARVO Annual Meeting Abstract, 2019), vol. 60, p. 1777.

31. J. L. Reiniger, A. C. Lobecke, R. Sabesan, M. Bach, F. Verbakel, J. de Brabander, F. G. Holz, T. T. J. M. Berendschot, W. M. Harmening, Habitual higher order aberrations affect Landolt but not Vernier acuity. *J. Vis.* **19**, 1–15 (2019).
32. E. G. González, A. M. F. Wong, E. Niechwiej-Szwedo, L. Tarita-Nistor, M. J. Steinbach, Eye position stability in amblyopia and in normal binocular vision. *Investig. Ophthalmol. Vis. Sci.* **53**, 5386–5394 (2012).
33. X. Zhu, W. He, Y. Du, K. Zhang, Y. Lu, Interocular symmetry of fixation, optic disc, and corneal astigmatism in bilateral high myopia: The Shanghai high Myopia study. *Transl. Vis. Sci. Technol.* **8** (2019), doi:10.1167/tvst.8.1.22.
34. J. Krauskopf, T. N. Cornsweet, L. A. Riggs, Analysis of eye movements during monocular and binocular fixation. *J. Opt. Soc. Am.* **50**, 572–578 (1960).
35. S. Polyak, Retinal structure and colour vision. *Doc. Ophthalmol.* **3**, 24–56 (1949).
36. N. Domdei, J. L. Reiniger, F. G. Holz, W. M. Harmening, Retinal factors of visual sensitivity in the human fovea. *bioRxiv* (2021), doi:10.1101/2021.03.15.435507.
37. R. Home, Binocular summation: A study of contrast sensitivity, visual acuity and recognition. *Vision Res.* **18**, 579–585 (1978).
38. C. Zhang, Y. J. Kim, A. R. Silverstein, A. Hoshino, T. A. Reh, D. M. Dacey, R. O. Wong, Circuit Reorganization Shapes the Developing Human Foveal Midget Connectome toward Single-Cone Resolution. *Neuron*. **108**, 905-918.e3 (2020).
39. L. R. Stanford, Conduction velocity variations minimize conduction time differences among retinal ganglion cell axons. *Science (80-.).* **238**, 358–360 (1987).
40. D. M. Dacey, The mosaic of midget ganglion cells in the human retina. *J. Neurosci.* **13**, 5334–5355 (1993).
41. G. Tan, Y.-H. Lee, T. Zhan, J. Yang, S. Liu, D. Zhao, S.-T. Wu, Foveated imaging for near-eye displays. *Opt. Express*. **26**, 25076 (2018).
42. H. Song, E. A. Rossi, D. R. Williams, Reduced foveal cone density in early idiopathic macular telangiectasia. *BMJ Open Ophthalmol.* **6**, e000603 (2021).
43. A. Roorda, F. Romero-borja, W. D. Iii, H. Qneener, Adaptive optics scanning laser ophthalmoscopy. *Opt. Express*. **vol**, 10pp405-412 (2002).
44. N. Domdei, L. Domdei, J. L. Reiniger, M. Linden, F. G. Holz, A. Roorda, W. M. Harmening, Ultra-high contrast retinal display system for single photoreceptor psychophysics. *Biomed. Opt. Express*. **9**, 157 (2018).
45. S. Poonja, S. Patel, L. Henry, A. Roorda, Dynamic visual stimulus presentation in an adaptive optics scanning laser ophthalmoscope. *J. Refract. Surg.* **21**, S575-80.
46. W. M. Harmening, W. S. Tuten, A. Roorda, L. C. Sincich, Mapping the perceptual grain

of the human retina. *J. Neurosci.* **34**, 5667–77 (2014).

47. D. W. Arathorn, Q. Yang, C. R. Vogel, Y. Zhang, P. Tiruveedhula, A. Roorda, Retinally stabilized cone-targeted stimulus delivery. *Opt. Express*. **15**, 13731 (2007).

48. D. Cunefare, L. Fang, R. F. Cooper, A. Dubra, J. Carroll, S. Farsiu, Open source software for automatic detection of cone photoreceptors in adaptive optics ophthalmoscopy using convolutional neural networks. *Sci. Rep.* **7**, 6620 (2017).

49. K. S. Bruce, W. M. Harmening, B. R. Langston, W. S. Tuten, A. Roorda, L. C. Sincich, Normal Perceptual Sensitivity Arising From Weakly Reflective Cone Photoreceptors. *Invest. Ophthalmol. Vis. Sci.* **56**, 4431–8 (2015).

Acknowledgments

General: We thank Austin Roorda and the members of his lab for kindly providing their image and PRL data for re-analysis.

Funding: We are grateful to have received third party research funding by the Carl Zeiss Foundation (HC-AOSLO), and the Emmy Noether Program of the German Research Foundation (DFG, Ha 5323/5-1).

Author contributions: JLR and WMH conceived the research idea. JLR, ND and WMH developed the data analysis pipeline. JLR performed the data analysis and convolutional neural network training. JLR and WMH wrote the manuscript. All authors discussed the results and edited the manuscript.

Competing interests: JLR: none, ND: none, FGH: none, WMH: none.

Figures and Tables

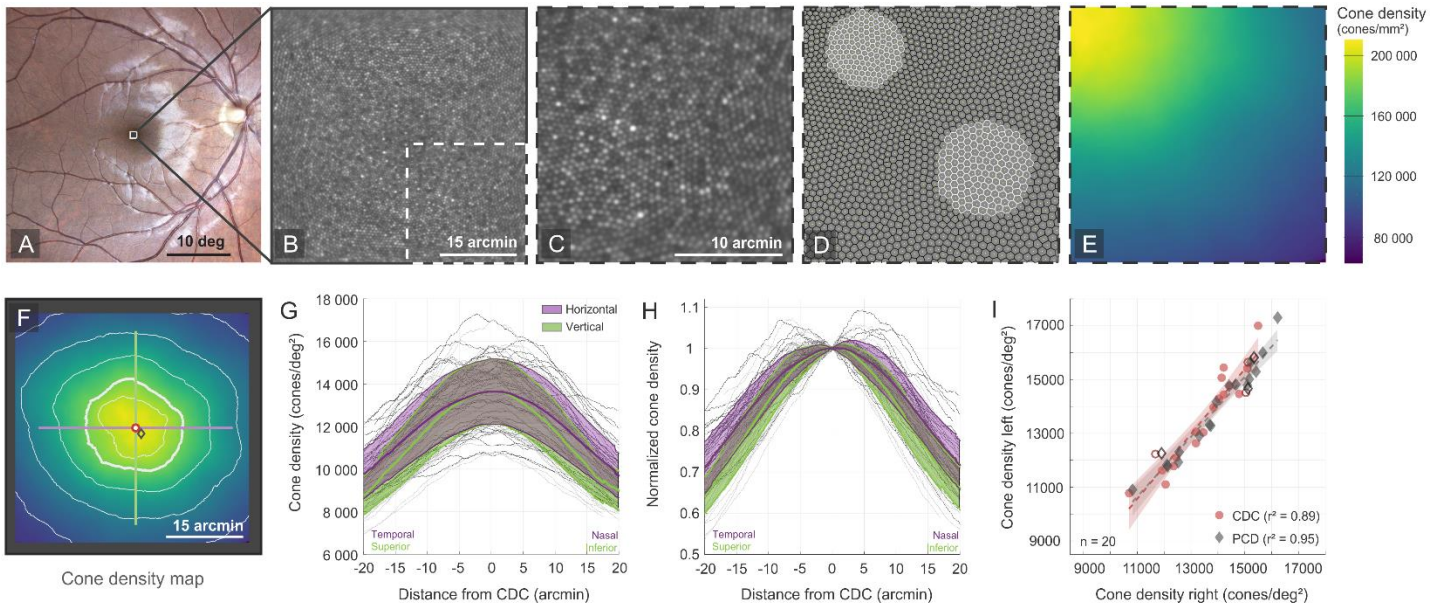

Fig. 1. Cellular topography of the foveola. (**A**) Fundus photography of a participants' right eye. The imaging field of view of the AOSLO, 51 arcmin, is shown as a white square. (**B**) Motion corrected and averaged AOSLO frames were used to create high-resolution topographical maps of all foveolar cones (B-F, for better visualization, the highlighted quadrant is shown enlarged in (C-E). (**C**) The enlarged quadrant of the cone photoreceptor mosaic with the smallest cells and densest cone packing in the upper left corner. (**D**) Voronoi tesselation of the semi-manually labeled cone coordinates was used for calculating continuous cone density based on the area of the nearest 150 Voronoi patches around each pixel in the image. (**E**) The resulting cone densities are visualized color coded, expressed here as cones/mm². (**F**) In the complete cone density map, iso-contour lines represent the 10th, 20th (bold), 40th, 60th and 80th percentile of density values. The cone density centroid (CDC) was determined as the weighted center of the 20th percentile of density values (red circle). The location of peak cone density (PCD) is shown by a gray diamond. The green and purple line indicate the meridians of profiles that were analyzed for all eyes and plotted in G and H. (**G**) Profiles of absolute cone density values (40 eyes of 20 participants), centered on the CDC, visualizing a large variety in absolute density values. (**H**) Same profiles normalized to cone density at the CDC. (**I**) Cone densities at the CDC (red dots) and PCDs (gray diamond) in fellow eyes of 20 participants were highly correlated ($r^2 = 0.89$, $p << 0.001$, and $r^2 = 0.95$, $p << 0.001$, respectively). Regression lines and 95% confidence intervals are represented by dotted lines and shaded areas, respectively.

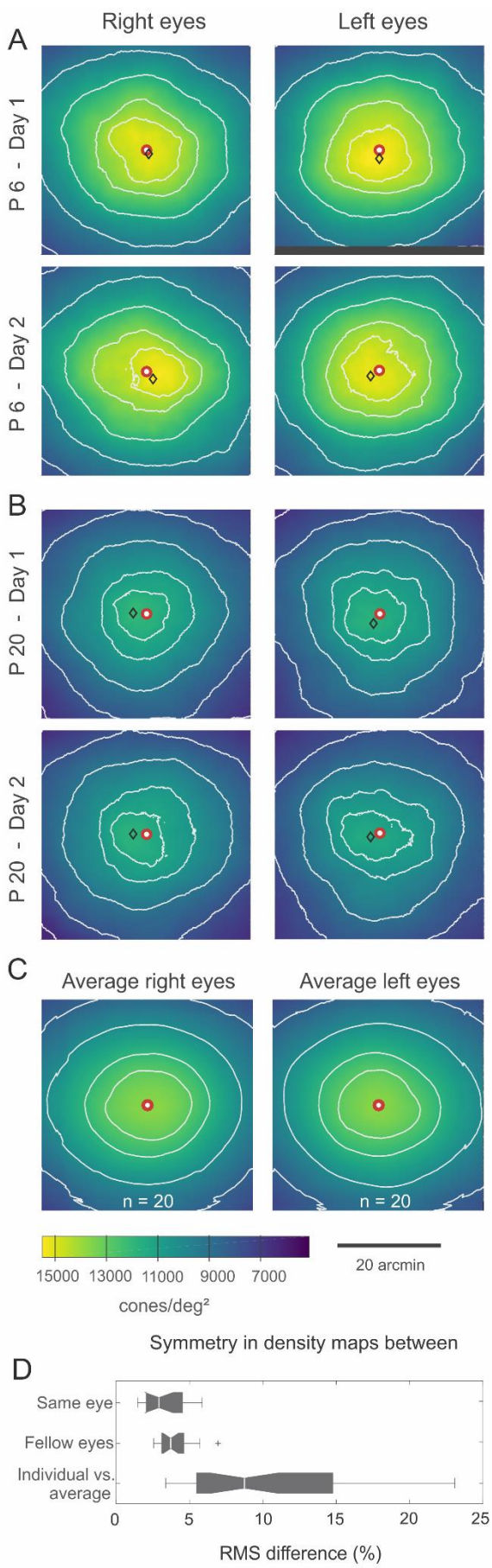

Fig. 2. Symmetry of foveolar cone density maps. (A+B) Cone density maps of both eyes of two participants (P6 and P20) shown in fundus orientation. Rows represent imaging sessions on different days. Contour line definition and marker (CDC and PCD) as in Fig. 1. (**C**) The spatially normalized and averaged cone density maps of all twenty right and left eyes in this study are shown in comparison. (**D**) The root mean square (RMS) of differences in absolute cone density values is shown in boxplots for the comparison of: same eyes on 2 different days, fellow eyes on the same day and individual eyes against the averaged cone density map of all eyes. The notch represents the 95% confidence interval of the median, box whiskers extend to the most extreme data values and plus markers represent outliers (distance from box > 1.5 x range between 25th and 75th percentile).

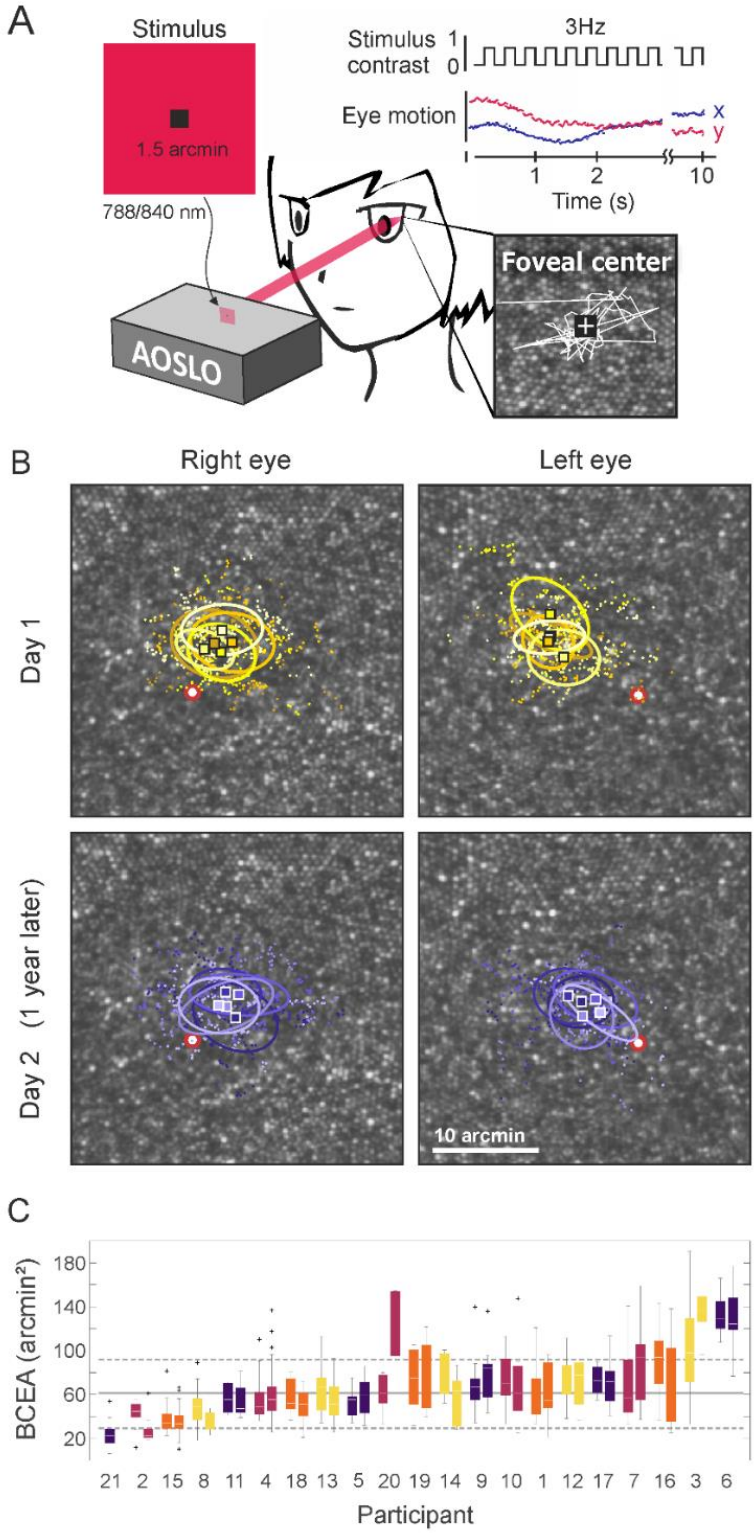

Fig. 3. Measuring fixation behavior. (**A**) The participant fixated a small flashing black square stimulus presented in the center of the imaging raster of the AOSLO (top right). High-resolution eye motion traces were derived from at least 5 consecutive, 10 sec AOSLO videos. (**B**) The PRL, computed as two-dimensional median of all stimulus locations, are shown for consecutive measurements in the right eye (left column) and left eye (right column) of P5 on two different days (~1 year between measurements) as square marker. Small dots indicate the retinal location of the stimulus in individual

video frames, color saturation represent consecutive videos. Ellipses are the area containing one standard deviation of the data (bivariate contour ellipse area, BCEA). The recorded 10 sec videos from both days were analyzed individually and combined, to measure variation over time (see also Fig. S.2). The CDC is visualized by a red circle with white fill. (**C**) BCEAs in all eyes per participants (numbers on abscissa), ordered by their average magnitude. The solid and dotted lines represent the mean value of all data and one standard deviation, respectively. Box whisker extend to the most extreme data values and plus markers represent outliers (distance from box > 1.5 x range between 25th and 75th percentile).

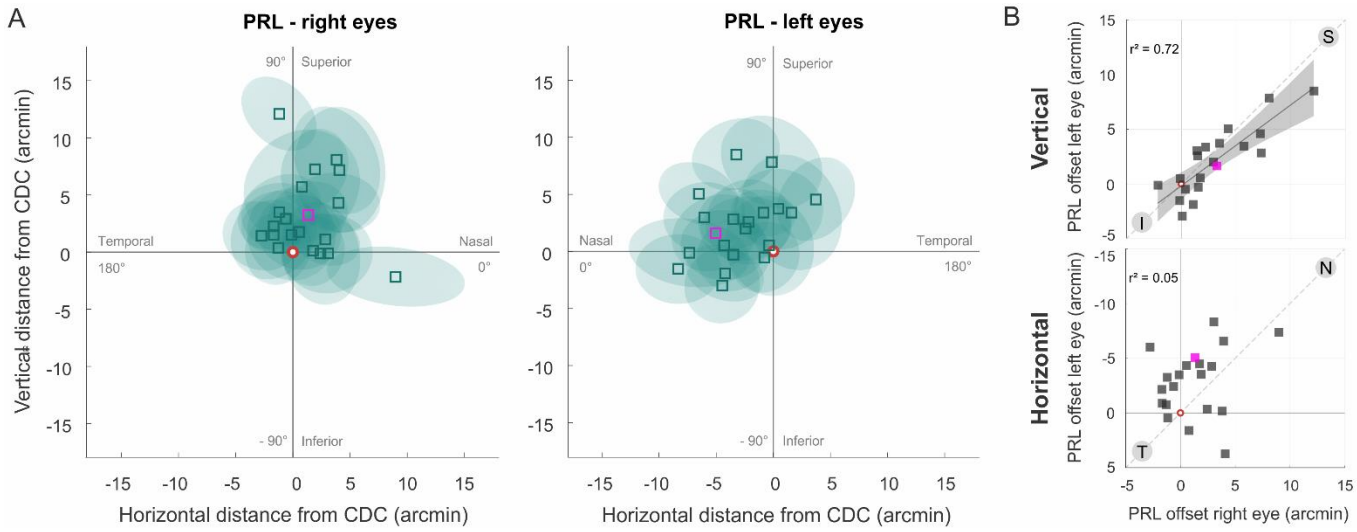

Fig. 4. Relationship between cone topography and fixation behavior. (**A**) The right and left eyes' PRL and fixation ellipse are plotted in fundus orientation, centered on the CDC. As an example, the PRL offsets of the participant whose offsets were most similar to the mean of the distributions (P13) are highlighted in purple in A, B and C. (**B**) The vertical offset components were strongly correlated between fellow eyes ($r^2 = 0.72$, $p << 0.001$). The regression line and the 95 % confidence interval are represented by a solid line and gray shaded area, respectively. The horizontal component showed a non-significant correlation between fellow eyes ($r^2 = 0.05$, $p = 0.32$). The dotted lines represent a perfectly mirror symmetrical offset between both eyes. S = superior, I = inferior, N = nasal, T = temporal retinal orientations.

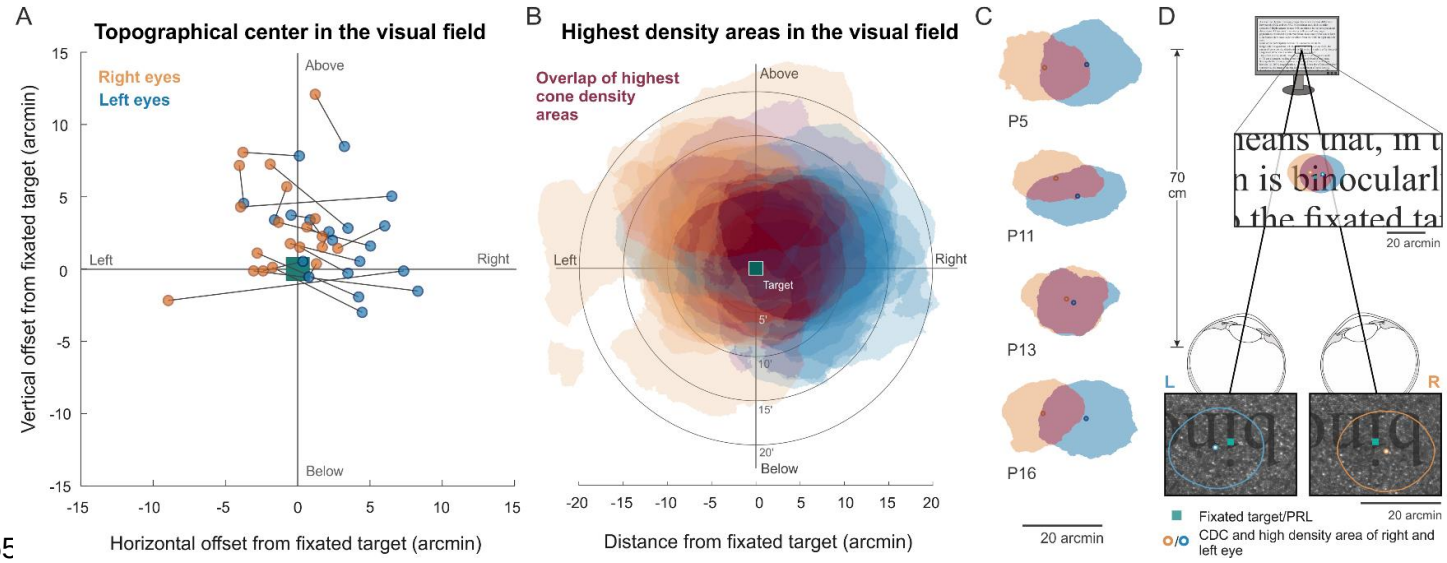

Fig. 5. Projection of cone topography into the binocular visual field. Monocular data are plotted together under the assumption of using the same retinal location under monocular and binocular viewing conditions. (**A**) The center of cone density distributions in relation to the location of the fixated target in the visual field. The lines connect fellow eyes of participants. Right and left eyes are plotted in orange and blue, respectively. (**B**) The areas encompassing the highest 20 % of cone densities (within the central 50 arcmin of the fovea) are projected to the visual field, relative to the fixated target. The overlapping area of fellow eyes is shown in dark red. High density areas are, on average, slightly offset towards details superior to the fixated object and displaced horizontally between eyes. (**C**) Four examples for individual overlaps between the highest density areas of fellow eyes were selected to reflect individual differences in size and direction of offsets between eyes. (**D**) The 20th percentile of highest density values for the average cone topography (Fig. 2C) is therefore offset from fixation in a way that the high density areas sample from overlapping, horizontally separated regions in the binocular visual field, with their centers separated by an amount equaling the distance between two letters at reading distance. The illustrated scene projects those areas from fellow eyes retinae (bottom) on a computer screen (top). The orientation of cone mosaics is as seen from behind the observer.

Supplementary Materials

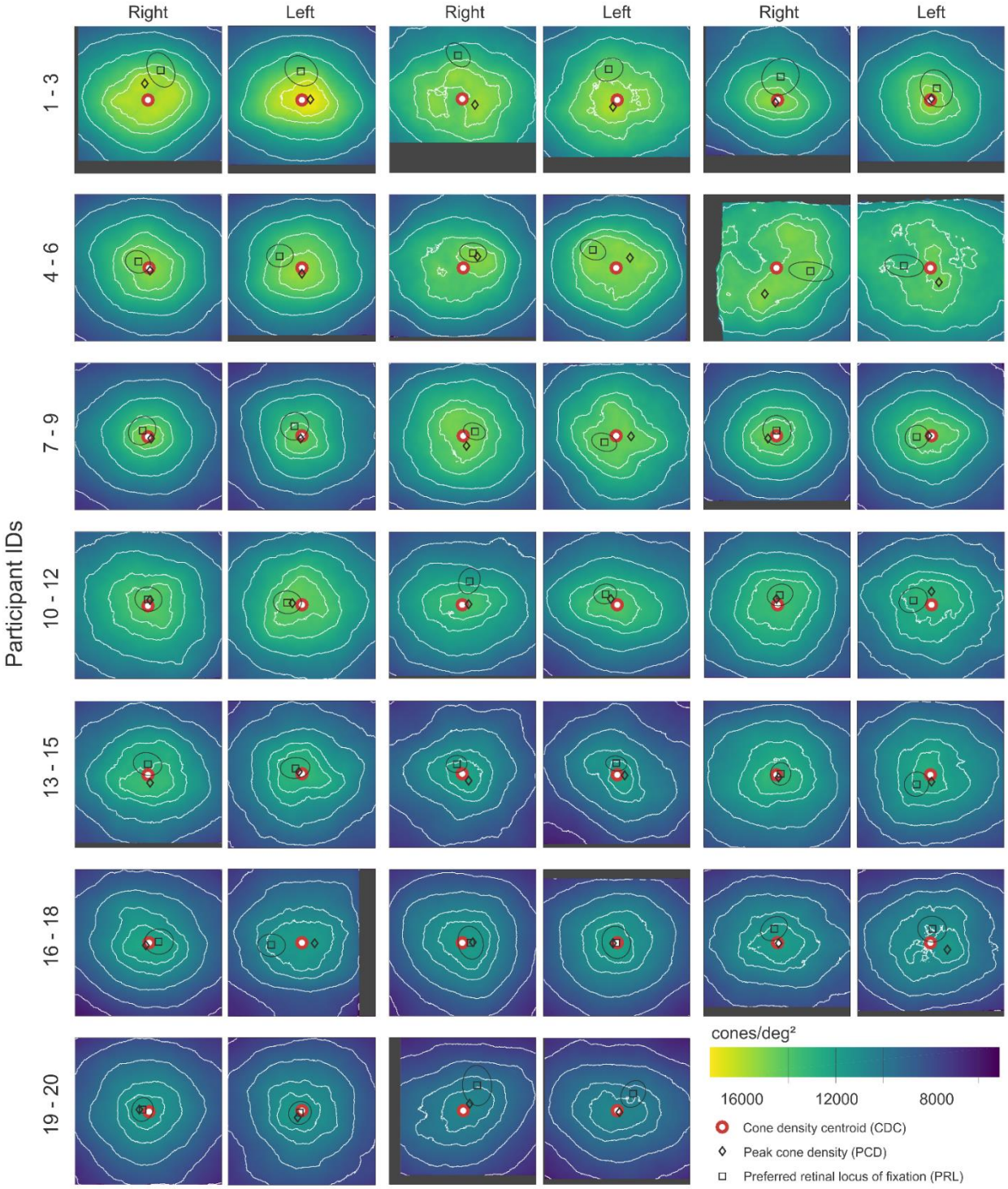

Fig. S1. Binocular cone density contour maps of all participants. The central 40 x 40 arcmin density maps of right and left eyes are presented in fundus orientation for all participants. Participants IDs (P1-P20) were ordered by PCD value exhibited, from top left to bottom right in this representation. Iso-contour lines represent the 10th, 20th, 40th, 60th and 80th percentile of density values. The cone density centroid (CDC) is indicated by a red circle. PCD = diamond, PRL = square, shown in the center of the individual fixation ellipse. Dark gray areas reflect parts of the image that were cropped because of borders or poor quality.

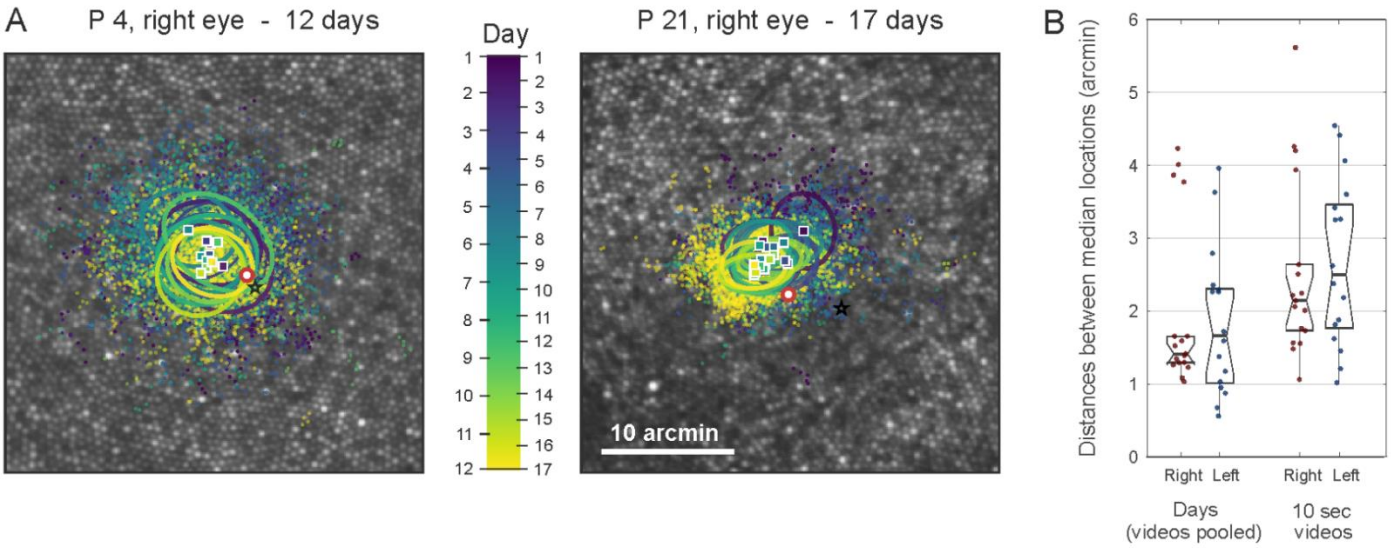

Fig. S2. Fixation stability across multiple years. (**A**) PRL measurements in two participants (P4 and P21) were recorded over a period of 3.5 years on 12 and 17 different days, respectively. Color represents measurement sessions and thus time between first and last examination (2017-2020). Small dots are individual stimulus locations, squares are PRLs shown inside their fixation ellipses. (**B**) The effect of data pooling compared between data taken from individual 10 sec videos and when pooled across multiple of such 10 sec videos recorded at the same day in all studied eyes.

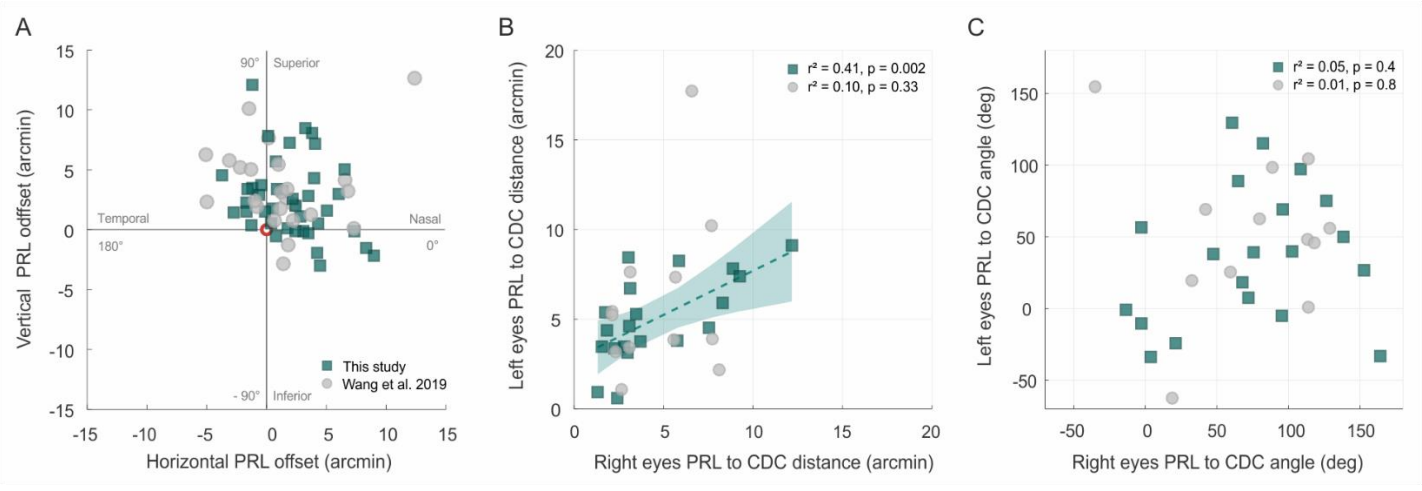

Fig. S3. PRL offsets in this study and re-analyzed data from Wang et al. (2019). (**A**) The right and left eyes' PRL relative to the CDC combined for both eyes (this study = squares, Wang et al. = circles). (**B**) Offset distance was significantly correlated between fellow eyes in our study ($r^2 = 0.41$, $p = 0.002$), but not in the data provided by Wang et al. ($r^2 = 0.1$, $p = 0.33$). (**C**) While demonstrating a similar trend, offset direction did not show a significant correlation between fellow eyes in either population (this study: $r^2 = 0.05$, $p = 0.36$; Wang et al.: $r^2 = 0.01$, $p = 0.76$).

Table S1. Participant statistics, ocular dominance, foveal cone mosaic metrics and PRL details. Ocular dominance was measured prior to PRL measurements. PCD and CDC densities are given in angular and linear units (retinal magnification was computed based on axial length, anterior chamber depth and retinal curvature for each eye). The PRL was measured on different days and PRL variability is the retinal distance between single repeated PRL measurements (runs), or pooled data across days. Note that in participant 21, the complete cone mosaic could only be resolved in the right eye.

				Cone mosaic				Fixation behavior					
Participant ID	**Gender**	**Eye**	**Dominance**	**PCD cones/deg²**	**PCD cones/mm²**	**CDC density cones/deg²**	**CDC density cones/mm²**	**# Measurement days**	**Total # of videos**	**PRL variability across single runs (arcmin)**	**PRL variability across days (arcmin)**	**Median BCEA (arcmin²)**	**Median BCEA across days (arcmin²)**
1	M	L	0	17309	210145	16997	206354	2	8	3.6	3.6	66.0	97.1
		R	1	16217	196477	15488	187643	2	8	5.6	3.9	68.1	105.2
2	F	L	0	16003	214584	15454	207225	2	10	3.3	4.0	43.0	75.0
		R	1	15667	210212	14217	190754	2	10	4.2	1.3	25.0	59.5
3	M	L	1	15814	217811	15650	215550	2	12	4.5	1.4	101.7	148.7
		R	0	15350	212760	15124	209632	2	12	3.9	4.2	136.1	162.8
4	F	L	0	15657	193441	15429	190622	3	15	1.9	2.3	47.7	57.8
		R	1	15230	190708	15101	189087	12	74	2.1	1.2	57.3	67.3
5	M	L	1	15301	207076	15058	203793	3	15	1.8	2.4	55.4	62.2
		R	0	15428	205507	14137	188313	3	15	1.5	1.6	61.0	69.6
6	F	L	1	15018	172925	14282	164448	2	10	3.3	1.6	132.3	154.6
		R	0	15157	170318	14030	157655	2	11	2.6	1.1	128.7	151.7
7	F	L	1	14828	198349	14774	197625	3	15	2.6	0.9	74.9	90.2
		R	0	14662	196147	14453	193346	3	15	2.2	1.3	73.2	101.3
8	F	L	0	14792	190964	14474	186860	2	10	2.4	2.3	46.6	65.6
		R	1	15102	188851	14789	184940	2	10	1.8	1.3	36.0	49.1
9	F	L	1	14763	207763	14433	203125	2	10	1.5	0.6	64.0	84.5
		R	0	14426	205894	14215	202877	2	9	2.5	1.4	79.0	92.4
10	M	L	0	14657	201831	14514	199867	2	13	3.4	1.2	72.4	108.6
		R	1	15126	207682	15035	206433	2	10	4.2	3.8	64.4	104.5
11	F	L	1	14175	187061	13971	184364	1	5	1.6	-	55.6	62.6
		R	0	13938	182418	13836	181085	1	5	2.2	-	47.3	76.4

				Cone mosaic				Fixation behavior					
Participant ID	**Gender**	**Eye**	**Dominance**	**PCD cones/deg²**	**PCD cones/mm²**	**CDC density cones/deg²**	**CDC density cones/mm²**	**# Measurement days**	**Total # of videos**	**PRL variability across single runs (arcmin)**	**PRL variability across days (arcmin)**	**Median BCEA (arcmin²)**	**Median BCEA across days (arcmin²)**
12	F	L	0	13315	150790	13069	148002	2	10	1.0	1.0	70.7	77.8
		R	1	13697	153715	13191	148042	2	10	2.2	1.0	77.5	87.7
13	M	L	0	13286	145870	13046	143232	3	16	4.1	2.8	68.0	86.3
		R	1	13733	148503	13470	145658	8	37	2.0	1.6	48.6	66.2
14	F	L	0	12897	176732	12640	173207	1	5	1.1	-	95.0	87.8
		R	1	13302	183331	13175	181574	1	5	2.8	-	63.6	69.2
15	F	L	0	12304	158973	12108	156444	3	15	1.6	0.7	29.5	46.7
		R	1	13381	169702	12449	157885	5	23	1.1	1.4	33.1	37.8
16	M	L	0	12259	162728	12233	162376	1	5	2.8	-	94.0	113.8
		R	1	11904	158460	11682	155512	1	5	2.4	-	85.9	119.4
17	F	L	1	11927	171912	11772	169675	3	15	2.2	2.3	73.9	78.0
		R	0	12524	179022	12363	176715	6	29	1.7	1.6	72.7	82.5
18	F	L	0	11818	163501	11617	160723	3	15	1.2	1.0	52.2	65.8
		R	1	12105	165061	11939	162803	3	15	1.6	1.3	47.8	56.6
19	F	L	0	11789	161489	11089	151900	2	10	4.4	1.7	74.8	99.4
		R	1	12131	168226	12053	167150	2	10	2.1	4.0	61.6	87.2
20	F	L	0	10894	159556	10761	157603	1	5	3.2	-	61.0	90.9
		R	1	10823	157559	10692	155656	1	5	4.4	-	100.1	150.7
21	M	R	1	18023	221889	16601	204383	17	62	1.5	1.5	23.2	29.0
			Median	14426	183331	14030	181574	2	10	2.2	1.5	64	85